

7-12-2021

# Fixed Bottom Wind Turbine Wave-Wake Interaction

Ondrej Fercak  
*Portland State University*

Follow this and additional works at: [https://pdxscholar.library.pdx.edu/open\\_access\\_etds](https://pdxscholar.library.pdx.edu/open_access_etds)



Part of the [Aerodynamics and Fluid Mechanics Commons](#), and the [Mechanical Engineering Commons](#)

Let us know how access to this document benefits you.

---

## Recommended Citation

Fercak, Ondrej, "Fixed Bottom Wind Turbine Wave-Wake Interaction" (2021). *Dissertations and Theses*. Paper 5732.

<https://doi.org/10.15760/etd.7603>

This Thesis is brought to you for free and open access. It has been accepted for inclusion in Dissertations and Theses by an authorized administrator of PDXScholar. Please contact us if we can make this document more accessible: [pdxscholar@pdx.edu](mailto:pdxscholar@pdx.edu).

Fixed Bottom Wind Turbine Wave-Wake Interaction

by

Ondřej Ferčák

A thesis submitted in partial fulfillment of the  
requirements for the degree of

Master of Science

in

Mechanical Engineering

Thesis Committee:

Raúl Bayoán Cal

Mark Weislogel

Gerald Recktenwald

Portland State University

2021

# 1 Abstract

The interest and benefits of offshore wind energy has also brought along legitimate design challenges for engineers. Most notably, the complex interaction between wind and turbine is further complicated by the addition of dynamic ocean waves. This dynamic coupling between wind, wave, and turbine is not fully understood. Experimentation and simulation have been used to characterize inflow and turbine wakes and separately, wind-wave interactions. But only simulations have just begun to look at the wind, wave, and turbine wake interaction, albeit with great difficulty. In this study, a scaled fixed-bottom wind turbine was placed in a custom wind tunnel containing a wave tank able to generate waves. Particle image velocimetry (PIV) was performed on three successive image planes in order to visualize wake development far downstream. The images were used to characterize the wave profile, wake center, and velocities. The data was used to decompose a standard ensemble mean further into phase-averaged means based on wave shape and location (phase). These decompositions were used to look at local phase-dependent trends for several quantities. The results illustrate that the wake profile is phase dependent and a wake pumping effect, due to the waves, is observed. Local momentum maxima, which are obscured by the ensemble mean, are revealed in the phase-averaged means at the wave crests. The waves do not transfer momentum, per se, but do convert streamwise momentum into vertical momentum. In addition, there is a phase-dependent oscillation in both the horizontal (streamwise) direction of the wake, as well as the vertical dis-

placement of the wake. The shear stress, advection, and turbulence terms show to have an imbalance along the vertical direction of the turbine. These results have implications for design optimization, siting, design, and power extraction.

# Contents

<b>1</b>	<b>Abstract</b>	<b>i</b>
<b>2</b>	<b>Introduction</b>	<b>1</b>
<b>3</b>	<b>Experimental setup</b>	<b>4</b>
<b>4</b>	<b>Methods</b>	<b>10</b>
<b>5</b>	<b>Theory</b>	<b>13</b>
<b>6</b>	<b>Results</b>	<b>15</b>
6.1	Streamwise Velocity . . . . .	16
6.2	Wake Recovery . . . . .	22
6.3	Wake Center Deviation . . . . .	23
6.4	Vertical Velocity . . . . .	25
6.5	Turbulent Shear . . . . .	29
6.6	Phase-Averaged Wave-Induced Reynolds Normal Stress . . . . .	32
6.7	Phase-Averaged Wave-Induced Reynolds Shear Stress . . . . .	35
6.8	Advection-Turbulence Profiles . . . . .	38
<b>7</b>	<b>Conclusion</b>	<b>40</b>
<b>8</b>	<b>References</b>	<b>44</b>

## 2 Introduction

Public demand for renewable energy, along with advances in research and technology, has driven an exponential increase in wind energy contribution to the global energy supply for the past two decades [13, 18, 25]. Offshore wind power is of particular interest due to several benefits. The turbines are less visible, they have higher wind speeds, and larger turbines are therefore more viable. Yet, there are many non-trivial design challenges to building an offshore wind farm.

For example, there is a well-studied interaction between the atmospheric boundary layer (ABL) and the turbine wake. The loss of momentum within the wake has a negative impact on power production for the downstream rows. This momentum deficit accumulates at each row and thus reduces total power density. The turbulent downstream interactions between parallel wakes can also cause additional momentum losses. Even further, these interactions can have implications on the net forces felt by the turbine and meteorological effects, just to name a few [17, 27, 2, 35, 21, 20]. These dynamics are critical for design purposes and are actively being explored for single turbines and wind farm arrays for both onshore and offshore applications.

For single onshore turbines, the wind-wake aerodynamics have been well explored by experimentation [8, 28, 12]. For instance, "The Wind Energy Handbook" by Burton *et al.* [8] provides an extensive outline of the history,

construction, power production, and theory used for turbine design. Crespo *et al.* [12] and Vermeer *et al.* [28] provide detailed overviews and analysis of different wake-modeling methods and power extraction physics, respectively. Advancements in large-eddy simulations (LES) have become integral to the study of turbine dynamics and have agreed nicely with single turbine, as well as wind farm, experimental results. Cal *et al.* [9], for example, independently supported the same mechanism experimentally that the results of Calaf *et al.* [10] were able to also capture using LES, which was regarding vertical kinetic energy flux as the primary mechanism for turbine kinetic energy from the ABL [32, 15, 14, 10, 29, 6, 9]. Wind-wake interactions have also been successfully modeled by LES for onshore wind farms [24, 34, 3]. Yang *et al.* [34], for example, compared favorably, a state-of-the-art LES to simulation to existing wind farm field measurements. For single turbines, experimental results showed good agreement with the wind-wake results for onshore wind farms [9, 5, 4].

Offshore wind-wake interactions are complicated by the dynamic coupling of the ocean wind and waves. There is a growing interest in this topic and high-fidelity simulation tools are being developed to study this air-water interface. Since the ocean wave is shifting phase over time, there is a temporal component to the air-sea interface, making it challenging to resolve in LES studies. To overcome this, the sea-air interface has been modeled as increasingly complex rough surface. Yang *et al.* [31] demonstrated that a dynamic model can be created using moving roughness elements as waves within a mul-

tiscale rough surface to model a turbulent boundary layer. Recently efforts are being made to resolve the time-varying water-interface in LES studies. For example, the study by Yang *et al.* [32] and as part of the ExaWind project at the National Renewable Energy Laboratory (NREL) [26]. In fact, Yang *et al.* [32] were able to build on their previous wind-wave results [33, 16] using LES to characterize the coupled wind-wave-wake interaction of an offshore wind farm. They found that “waves have an appreciable effect on the wind farm performance” [1, 32]. In a later work Xiao *et al.* [30] performed a triple-decomposition, similar to Buckley *et al.* [7], to decompose not only the turbulent fluctuations from the mean (Reynolds decomposition), but also decomposed the phase-averaged mean from the ensemble mean to define an instantaneous phase-averaged dependent fluctuation term. However, to date there has been no experimental validation of this coupled wind-wave-wake interaction, and further investigation is necessary to understand better the effect of ocean waves on the wake recovery in large offshore wind farms.

Recently, Akervik *et al.* [1] studied turbulent flow over monochromatic waves by means of wall resolved LES. The offshore wind-wave dynamics are difficult to study experimentally due to the need for a wind and water tunnel with sufficiently long fetch to develop wind-driven waves, and because of challenges related to Froude and aerodynamic scaling. Nevertheless, many in situ experimental measurements of wind driven waves have been performed [11, 22]. Most notably, Buckley *et al.* [7] showed direct evidence of turbulent events between airflow and surface waves through PIV and light induced

fluorescence (LIF) measurements. The natural extension of this research is to combine well developed techniques for studying scaled turbine wind-wake dynamics, with experimental techniques for simulating offshore wind-wave dynamics in a wind- and water tunnel.

The present study aims to investigate the coupled wind-wave-wake interaction for a scaled single fixed-bottom wind turbine. A fixed bottom turbine was selected to isolate the three main variables from the additional frequency dynamics of a floating turbine. Understanding the dynamics of a single turbine was preferred as an important building block with which future work can be extended for large wind farms. A traditional 2D PIV wind tunnel experimental set-up was modified with a water wave tank and wave generator, to simulate long-period deep-water ocean waves. Streamwise velocity results were obtained across three PIV planes to capture the full turbulent wake evolution from approximately  $0.75D$  to  $5.25D$  downstream. Mean velocity fields, as well as the conditionally averaged velocity fields based selected streamwise wave phases, were calculated. The momentum results, Reynolds stresses, wake deficit, wake-center deviation, and momentum budget were then analyzed.

### **3 Experimental setup**

The experiments of a scaled fixed bottom wind turbine were performed in the closed-loop wind and water tunnel at Portland State University. For

this purpose, the wind tunnel floor was replaced with a customized water-tank to simulate deep ocean wave conditions. The wind tunnel test section had a height of 0.8 m, width of 1.2 m and test-length of 5 m. Based on the wind tunnel size, a diameter of 0.15 m was selected for the scaled wind turbine, resulting in a geometric scaling ratio of 1:600 in comparison to a full scale turbine with a diameter of 90 m. The water tank covered the full wind tunnel floor and provided a water depth of 0.3 m, corresponding to a water depth of 180 m in full-scale. The tank was isolated from the wind tunnel to reduce vibration and was supported with anti-vibration leveling feet. The side-walls were assembled of schlieren-grade annealed float glass fastened to the aluminum framework to ensure maximum access for the laser and camera hamilton2015wind, asejev2016vortex, ali2018assessing, bossuyt2021quantification. The wind tunnel speed had a range between 2 and 40  $\text{ms}^{-1}$ . The tunnel ceiling was configured to approach a zero-pressure gradient boundary layer. A wave paddle was positioned at the entrance of the test-section, and was controlled by a stepper motor to produce scaled long-period deep-water waves. At the end of the test-section a custom made static wave damper was used to absorb the incoming waves.

Each wind and wave condition was measured using LIF [7]. A FLIR BFS-U3-51S5M camera with a 532 nm optical filter in combination with a 200 mW, 532 nm, continuous LED laser sheet and a commercially available red fluorescent dye was used to track the water surface. A cropped region of interest was acquired using the camera sensor to cover only the region where

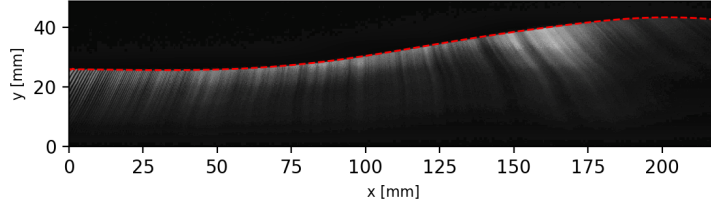


Figure 1: Example of image used for wave identification recorded by LIF. Example given for the short period wave condition.

the water height was visible enabling a sampling rate increase to 250 Hz. Figure 1 shows an example of a recorded image for wave shape identification. Using standard image processing techniques, the wave height was deduced from each image. The wave period was found from the frequency spectrum of wave height at a fixed location, and the wave-velocity from the time-lag corresponding to the maximum correlation between wave height of two points with maximum separation in the field of view. The uncertainty of the wave period was estimated from the sampling frequency to be  $\pm 0.01$  s. The uncertainty of wave speed was estimated from the sampling frequency, distance between the two points, and the measured velocity itself. The wavelength and its uncertainty were derived from the measured wave period  $T$  and speed  $V$ , according to  $\Lambda = VT$ . Three different wave conditions were considered in this study including a no-wave condition. The two active wave conditions were governed by the constant rotational speed of the wave paddle, resulting in waves with a measured period of  $(0.5 \pm 0.01)$  s and  $(0.8 \pm 0.01)$  s. The measured wave speeds generated by the paddle are  $(0.7 \pm 0.03)$  m/s and  $(1.2 \pm 0.08)$  m/s, and the measured wavelengths were  $(0.36 \pm 0.02)$  m and

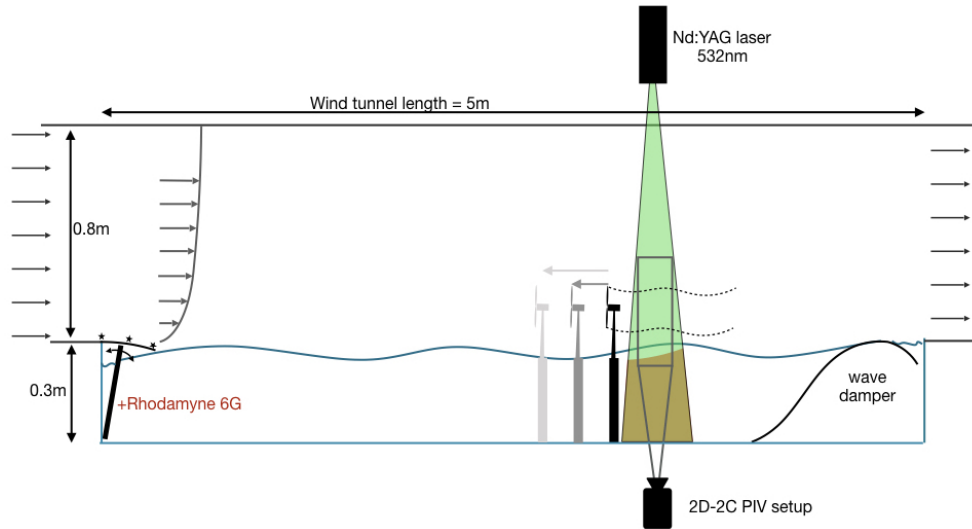


Figure 2: Schematic representation of the experimental setup. Image not to scale.

( $1 \pm 0.06$ ) m, see Table 1. On top of the long period waves generated by the wave paddle, small scale wind driven waves were generated depending on the wind conditions. Considering the water depth of 0.3 m, the two smallest generated waves were considered deep water waves, while the longest generated wave was on the limit of the general criteria for deep water waves:  $h/\lambda > 0.5$ , with  $h$  the water depth.

Particle image velocimetry was used to measure 2D-2C velocity fields in streamwise aligned planes. The PIV setup consisted of a 4 megapixel CCD camera and a Litron Nano double pulsed Nd:YAG (532 nm, 1200 mJ, 4 ns duration) laser. The camera lens had a focal length of 50 mm. Neutrally buoyant fluid particles of diethyl-hexyl sebacate were aerosolized by a seeding generator with a constant density throughout the experiment. For each mea-

surement 3000 independent image-pairs were recorded at a frequency of 4 Hz. DAVIS 8.4 software was used to apply a multi-pass Fast Fourier Transform (FFT) based cross-correlation algorithm and a universal outlier detection method to filter out unwanted vectors from the PIV data. A multiple-pass reducing size interrogation window of  $64 \times 64$  pixels and  $32 \times 32$  pixels, with a 50% overlap was used to process the data. The PIV window covers an area of  $0.2 \text{ m} \times 0.2 \text{ m}$ . Three planes were measured in the wake of the turbine by changing the relative position of the scaled wind turbine model compared to the location of the fixed PIV measurement plane. The PIV measurements of the wake covered a downstream distance of  $x/D = 1 - 5$ , as indicated in Figure 2. Time averaging was approximated by ensemble averaging over all PIV snapshots. Conditional averaging of the PIV images with regards to the wave phase is discussed in the next section.



Figure 3: Photograph of the experimental setup with long-period waves and super-imposed wind generated waves.

The scaled wind turbine was positioned on a stiff support made of  $25 \times 50$

mm aluminum profile which reached up to just below the water surface. The scaled wind turbine used the rotor design from Odemark *et al.* [19], which was geometrically scaled to a diameter of 0.15 m. The rotor blades were 3D printed using a 3D Systems ProJet MJP 3600 in high detail resin and the turbine tower using a Formlab 2 SLA 3D printer. A Faulhaber 1331T012 DC motor was used as a DC generator to control the tip speed ratio. The tip speed ratio of TSR=5 during the measurement was selected for a maximum power coefficient, which was estimated using the motor constants provided by the manufacturer of the DC motor to be  $c_p \approx 0.25$ .

Table 1: Experimental Design Parameters

<b>Rotor</b> Diameter	<b>Wind</b> Speed	<b>Wave</b>					
		Frequency	Period	Amplitude	Speed	Wavelength	
0.15m	2.6 m/s	2.00 Hz	0.5 s	0.020 m	0.7 m/s	2.33D	0.36 m
-	5.9 m/s	1.25 Hz	0.8 s	0.013 m	1.2 m/s	6.67D	1.00 m

## 4 Methods

In order to determine the phase-averaged velocity field  $u_\phi$ , a baseline wave shape was established for each of the two wave frequencies  $\lambda_m$ , where  $m$  is 1.25 Hz or 2 Hz. For this purpose, the wave conditions without wind were measured with the FLIR camera and continuous LED laser, as described in the experimental setup.

The extracted wave shape outline for each of the two wave conditions was segmented into distinct peak-to-peak wavelengths and averaged into a single waveform. This baseline waveform was used to build the two continuous waveforms,  $\gamma_m$ , long enough to span all three PIV planes, and smoothed using a 3 order polynomial Savitzky–Golay filter with a 5.4 mm window length [23]. The amplitude and wavelength was then scaled to that of the PIV data and the vertical shift was adjusted so the zero-crossing of the wave profile was at water height. The horizontal shift was adjusted so that the wavelength in 1 position,  $\gamma_m(\phi_1)$ , was always at a crest for  $x/D = 1.5$ . A total of four phases,  $\phi_k$ , were considered where  $k = 1 : 4$ , for each wave condition  $\gamma_m(\phi_k)$  at:

$$\gamma_m(\phi_k) = \gamma_m(\phi_1) + \frac{\lambda_m}{4}(k - 1). \quad (1)$$

The wave profiles  $\gamma_{m,n,d}$  for all snapshots, where  $d$  is the snapshot index number from 1 : 3000, were then compared to the baseline profile  $\gamma_m(\phi_k)$  for each phase number using the absolute area between the two curves for each

PIV plane:

$$\delta_{m,n,d} = \int_{x_1}^{x_2} \gamma_m(\phi_k) - \gamma_{m,n,d} dx, \quad (2)$$

where the bounds for the definite integral  $x_1$  and  $x_2$  were defined as the left and right streamwise x-position for each  $\gamma_{m,n,d}$ . A fit value  $\delta_{m,n,d}$  was assigned to each image for further processing.

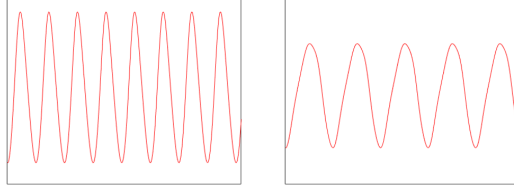


Figure 4: Normalized mean wave profiles used as baseline for analysis: a) 2 Hz wave condition, and b) 1.25 Hz wave condition.

Separate thresholds,  $\zeta_{m,n}$ , were established for each wave frequency,  $m$ , and wind speed,  $n$ , combination, where  $n$  is 2.64 m/s or 5.88 m/s. The snapshots with fit value  $\delta_{m,n,d}$  smaller than the threshold,  $\zeta_{m,n}$ , were collected in an array  $\delta'_{m,n}$ :

$$\delta'_{m,n} = \delta_{m,n,d} \leq \zeta_{m,n} \quad (3)$$

The phase-averaged snapshots, with length  $N_{m,n}$ , in  $\delta'_{m,n}$  were used to create the phase-averaged velocity fields for both the horizontal x-direction  $\bar{u}_\phi$ , and vertical y-direction  $\bar{v}_\phi$ :

$$\bar{u}_\phi(x, y; \phi) = \frac{1}{L} \sum_{l=1}^L \delta'_{m,n} \quad (4)$$

The average number of snapshots for each case was 218 with a minimum number of 91 and a maximum number of 336.

The wake center for the turbine was calculated for each of the 3000 instantaneous snapshots. To remove noise near the wave, points below wave height plus 10 pixels were eliminated for each snapshot. Similarly, any points above  $y/D = 1.25$  were removed due to noise from entrainment and tip vortices. For the points within these bounds, the point of minimum velocity for each horizontal ( $x$ ) position was found and then averaged. The results are plotted as a red line in Figure 5. Additionally, the standard error ( $SE$ ) was calculated:

$$SE_{\mu_\phi} = \frac{S}{\sqrt{N}}, \quad (5)$$

where  $SE_{\mu_\phi}$  is the standard error of the mean for each experimental case,  $S$  is the standard error for each case, and  $N$  is the number of snapshots for each case. The standard error is overlaid as a hatch-pattern on top of the wake center lines in Figure 5.

The wake recovery was found at each corresponding wake center position as  $\bar{u}/\bar{u}_\infty$  and  $\bar{u}_\phi/\bar{u}_\infty$  shown in Figure 6. Similarly, the wake center deviation was calculated for each case by finding the deviation ( $\Delta$ ) from the turbine hub height and normalized by the blade diameter ( $D$ ) as  $\Delta/D$ .

## 5 Theory

In order to quantify the relevant terms for analysis, we begin with the Reynolds-averaged Navier-Stokes (RANS) equations for steady, incompressible, and inviscid flows:

$$\overline{u_j} \frac{\partial \overline{u_i}}{\partial x_j} = -\frac{1}{\rho} \frac{\partial \overline{p}}{\partial x_i} - \frac{\partial}{\partial x_j} \overline{u'_i u'_j} - f_{x_i} \quad (6)$$

where  $x_i$  is the streamwise, vertical, and transverse coordinates  $x$ ,  $y$ , and  $z$  respectively. Similarly,  $u_i$  are the velocity vectors in the streamwise, vertical, and transverse directions  $u$ ,  $v$ , and  $w$ . Components with an overbar denote time averaging and components with primes indicate turbulent fluctuations. The pressure is  $p$  and  $\rho$  is the fluid density. The forcing term  $f_{x_i}$  denotes the thrust of the wind turbine. Viscous terms are neglected since the flow is considered far from solid boundaries, and the time derivative is excluded from the material derivative on the left side of the equation since the flow is considered steady.

Due to the 2D experimental set-up, we consider only the streamwise, or  $x$ -direction, momentum equation with streamwise and vertical coordinates  $x$  and  $y$ . This simplifies Eq. 6 to:

$$\underbrace{\overline{u} \frac{\partial \overline{u}}{\partial x} + \overline{v} \frac{\partial \overline{u}}{\partial y}}_{\text{advection}} = -\frac{1}{\rho} \frac{\partial \overline{p}}{\partial x} - \underbrace{\frac{\partial}{\partial x} \overline{u' u'} + \frac{\partial}{\partial y} \overline{u' v'} + \frac{\partial}{\partial y} \overline{v' v'}}_{\text{turbulence}} - \overline{f_x} \quad (7)$$

where the left hand side of the equation indicates the advection terms. The

$\overline{u'v'}$  is the Reynolds shear stress and  $\overline{u'u'}$  and  $\overline{v'v'}$  are the Reynolds normal stresses in the streamwise and vertical direction, respectively. These Reynolds stresses, or turbulent momentum fluxes, comprise the turbulence terms indicated on the right hand side of the equation.

To evaluate the decoupling of waves, wake and inflow interactions, a phase-averaged decomposition similar to Buckley *et al.* [7] given the phase dependence of the waves and its possible influence on the flow above. A standard Reynolds decomposition using the phase-averaged mean is applied as:

$$u_\phi(x, y) = \bar{u}_\phi(x, y; \phi) + u'_\phi(x, y), \quad (8)$$

where  $u$  is the instantaneous velocity,  $\bar{u}_\phi(x, y, \phi)$  is the phase-averaged mean velocity, and  $u'(x, y)$  is the fluctuation term. The streamwise direction continues to be  $x$ , similarly with the  $y$  being the wall-normal direction and the wave phase is  $\phi$ .

In a similar manner, a relationship between the phase-averaged mean velocity  $\bar{u}_\phi(x, y, \phi)$  and the ensemble mean  $\bar{u}(x, y)$  can be posed while now introducing a phase-averaged deviation  $\tilde{u}(x, y, \phi)$ :

$$\bar{u}_\phi(x, y; \phi) = \bar{u}(x, y) + \tilde{u}_\phi(x, y; \phi). \quad (9)$$

Combining Equation (8) and Equation (9), the following triple decomposition is obtained:

$$u_\phi(x, y) = \bar{u}(x, y) + \tilde{u}_\phi(x, y; \phi) + u'_\phi(x, y). \quad (10)$$

This decomposition is necessary to show that these terms are related quantities. In other words, the phase-averaged mean  $\bar{u}_\phi(x, y; \phi)$  is not isolated from the ensemble mean  $\bar{u}(x, y)$ , but instead is a composition of the ensemble mean  $\bar{u}(x, y)$  (averaged over all phases) and a phase-averaged deviation  $\tilde{u}(x, y; \phi)$ . This is analogous to the Reynolds decomposition in Equation (8), which combined with Equation (8) shows that the phase-averaged mean, ensemble mean, instantaneous velocity, and instantaneous fluctuation are indeed all related. Eq.10. The equations outlined in this section are the foundation for the analysis and discussions in the next section.

## 6 Results

Understanding wake deflection and recovery can lead to improved turbine models. Wake deflection and recovery can be better understood by characterizing their phase dependence in the offshore case given the obvious boundary condition imposed at the surface. This understanding can provide enhanced mechanisms of energy production and control schemes.

In this section, the time-averaged ensemble means for the streamwise velocity, vertical velocity, and Reynolds shear stress are investigated to characterize the dominant terms in the Reynolds Averaged Navier Stokes (RANS) equation, and reveal their possible dependence on the phase characteristics,

thus evaluating the phase-averaged terms from Eq.(10). Further, the wake recovery, wake deflection and a momentum budget are pursued providing a quantification of the influence due to the waves and their position. This quantification can assist in possible strategies to improve power production and siting considerations.

More specifically, the wake center deviation aids phase dependent effect quantification on the wake. This is considered by visualizing the vertical position of the wake center in the streamwise direction. The measurement spans three consecutive PIV windows spanning  $4D$  downstream and  $1.2D$  vertically. The inflow is advected from left to right and the turbine origin is located at  $x/D = 0$ . Time averaged  $\bar{u}$  and phase-averaged  $\bar{u}_\phi$  streamwise mean velocities are presented in Figure 5 for two wave frequencies as outlined in Table 1.

## 6.1 Streamwise Velocity

Figures 5.a and 5.b show the ensemble-averaged streamwise velocity profiles ( $\bar{u}/\bar{u}_\infty$ ) for wave frequencies of 2 Hz and 1.25 Hz, respectively. The overall wake profile looks as expected based on previous work by, with a region of reduced momentum directly behind the turbine hub which slowly recovers downstream. As the wake moves downstream, the wake center drifts down toward the water line. This effect is present for both wave frequencies but is slightly more pronounced for the longer wave-length in Figure 5.b. This effect is known to be due to the vertical shear ( $\overline{u'v'}$ ) in mean velocity and may be

counteracted by the increased frequency of the shorter wave length in Figure 5.a. Both phenomena are discussed in more detail in the following sections. High velocity regions can also be seen near the wave and turbine (lower-left) in both figures. However, in Figure 5.a, this region extends a shorter lateral distance and is lower in magnitude than is seen in Figure 5.b. This disparity is likely due to the larger disruption of the inflow from high frequency (2 Hz) waves in Figure 5.a versus the long wave length (1.25 Hz) in Figure 5. It is worth noting that the low frequency (1.25 Hz) wave has a greater wave speed (1.2 m/s) compared to the high-frequency (2 Hz) wave speed (0.7 m/s). The free-stream velocities (2.6 m/s and 5.9 m/s) were significantly greater than either wave speed. However, to illustrate the importance of this point, any velocity  $u/u_\infty < 0.12$  for the shorter wave frequency (2 Hz) is moving slower than the wave itself (Fig. 5.a, 5.c, 5.e, 5.g, and 5.i). For Figures 5.b, 5.d, 5.f, 5.h, and 5.j, any velocity  $u/u_\infty < 0.2$  is moving slower than the wave. This implies that, as wave speeds approach that of the free-stream ( $\bar{u}_\infty$ ) velocity, there is a higher likelihood that the wave itself can impart momentum into the system versus simply acting as a moving obstruction.

Figures 5.c and 5.d show the conditional phase-averaged velocity means ( $\bar{u}_\phi/\bar{u}_\infty$ ) for phase 1. As before, Figure 5.c displays the short wavelength (2 Hz) and 5.d displays the longer (1.25 Hz) wavelength. The wake-centers follow the phase-locked wave profiles through the contours. This is more pronounced in Figure 5.c, where the wave undulations distort the wake much more than in Figure 5.d. This is most noticeable in the low-velocity wake

pocket between the two wave crests in Figure 5.c. Even though the wake center deviation in Figure 5.d is less pronounced, it still has the same concavity as the wave shape, as is seen for all phases in the following sections. The waves therefore, at a minimum, have a vertical impact effect as far as the turbine hub height, which, for the long-period wave, is 8 times higher than the wave height. The high velocity region near the wave and turbine (lower-left) in Figures 5.d is located at the crest of the phase 1 wave ( $x/D = 1$ ) as expected but the magnitude and lateral extension is similar to that of the ensemble mean (Fig. 5.b). However, Figure 5c reveals a dramatic difference in the comparable high-velocity region. While the location is also at the crest of the wave, the magnitude is much greater. Note that the wake meanders vertically as a function of the wave phase.

In the case of the shorter wave-length (2 Hz) in Figure 5.c, multiple wave crests are seen. The high-velocity region in question ( $x/D = 1.5$ ) is reduced for the second wave crest ( $x/D \approx 4$ ), but still exhibits a region of high velocity. These regions of high and low velocities at the crests and troughs are not unexpected for a phase-locked wave, which acts as an obstruction (assuming the wave speed is lower than the wind speed, as discussed above). However, what is unexpected, is that the ensemble-average in Figure 5.a provides virtually no indication of the significant localized wind velocities near the wave crests when the phase-averaged velocities are decomposed, as seen in Figures 5.c, 5.e, 5.g, and 5.i.

The phase-averaged 2 Hz velocity profiles ( $\bar{u}_\phi/\bar{u}_\infty$ ) for phases 1-4 are

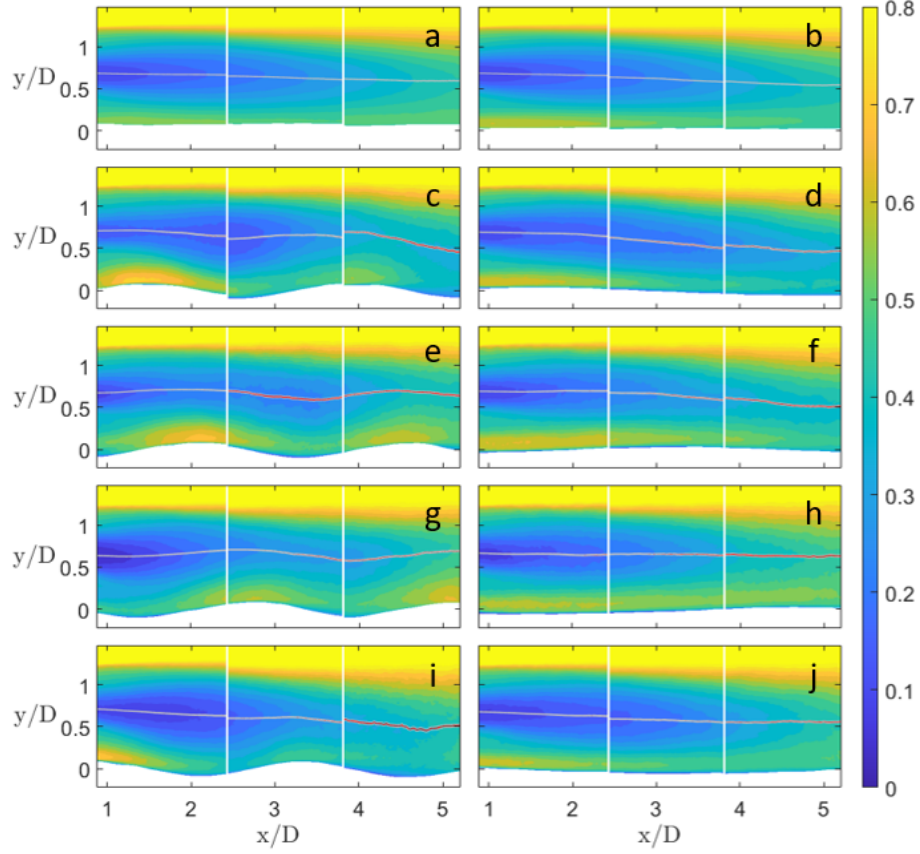


Figure 5: Normalized streamwise velocity profiles for 5.9 m/s inflow: (a) ensemble-average for 2 Hz wave and (b) ensemble-average for 1.25 Hz wave and (c) phase-average,  $\phi = 1$ , for 2 Hz wave and (d) phase-average,  $\phi = 1$ , for 1.25 Hz wave and (e) phase-average,  $\phi = 2$ , for 2 Hz wave and (f) phase-average,  $\phi = 2$ , for 1.25 Hz wave and (g) phase-average,  $\phi = 3$ , for 2 Hz wave and (h) phase-average,  $\phi = 3$ , for 1.25 Hz wave and (i) phase-average,  $\phi = 4$ , for 2 Hz wave and (j) phase-average,  $\phi = 4$ , for 1.25 Hz wave.

presented in Figures 5.c, 5.e, 5.g, and 5.i, respectively. The wake center and wake deficit continue to be influenced by a pumping behavior as the wave moves through each of its phases. When the wave crest is close to the turbine it displaces the flow up, resulting in a speed up near the wave and a reduction

in the wake strength. Then as the wave is moving downstream, this speed up follows the wave. However, the wake is traveling faster than the wave. Yet it is also observed that downstream the wake shape is modulated by the waves in a dynamic way. This pumping behavior results in faster wake recovery which is investigated in the next section. The high-velocity region at the crest of the first wave ( $x/d = 1.5$ ) in Figure 5.c continues to be present at that crest with diminishing intensity as seen in Figures 5.e, 5.g, and 5.i. However, if the second wave crest is followed from Figures 5.c, 5.e, 5.g, and 5.i then the velocity values at the crest become stronger again. So there is a phase-averaged space dependent behavior of this speed up, synchronised with the turbine location. What is clear is that the low-velocity regions in the wake are extended successively in Figures 5.e, 5.g, and 5.i. Figure 5.i depicts a low velocity wake region much shorter than in Figure 5.g. This suggests that the recovery of a wind turbine wake with waves is not uniform. The wake has an undulating effect, which is also explored more in further sections. Due to the waves, the wake is pumped downstream and eventually shed, as in Figure 5.i, which helps explain the apparent lack of high-velocity regions for certain phases.

Even though the longer period (1.25 Hz) full wave-length (6.67D) is longer than the PIV window, the wake center also follows the wave shape well (Fig. 5.d, 5.f, 5.h, and 5.j). For example, Figure 5.f exhibits a concave wave and corresponding concave wake-center while Figure 5.j exhibits a convex wave and wake-center pair. The wake profile is elongated and not as distorted due

to the wake pumping described above. The high velocity regions near the wave and turbine (lower-left) are elongated in Figures 5.d, 5.f, and 5.h but resemble the ensemble-mean in Figures 5.b much more than the comparable Figures 5.a, 5.c, 5.e, 5.g, and 5.i). This elongation of the high-velocity region for the long-period (1.25 Hz) wave follows the wave crest as for the short-period (2 Hz) wave, but extends more to the leading edge of the wave (wave orientation is defined from the air inflow direction) into the wave trough, as can be seen in Figures 5.f.

Since the wake is phase dependent and pumping is present, there is an oscillation dependence that plays a role in structural considerations, mechanical design, and energy extraction. From a structural perspective there would be an imbalance between the upper and lower sections of the turbine creating additional torque on the blades, rotor shaft, and therefore the tower itself. This could help explain the insidious nature of tower strikes. The natural frequency of the blades may need to be considered as to not align with the pumping frequency and avoid resonance. The undulating nature of the wake and momentum acceleration would mean that the life-cycle of the mechanical components could be overestimated. It also suggests that the vertical motion of floating wind farms may help align these imbalances. The pumping effect simultaneously shows a reduction in time-averaged wake momentum, specifically near the wave, but also reveals a large localized increase in momentum. The former implies that turbines could be spaced closer together. However, the latter clarifies that turbine spacing should not necessarily be

reduced because there is a higher momentum in the phase-average, which is masked by the ensemble-average.

## 6.2 Wake Recovery

The wake recovery is shown in Figures 6.a and 6.b. Points selected at 0.5 increments of  $x/D$  and spanning 4D are used to display wake center recovery for both waves. For the 2 Hz wave condition, Figure 6.a demonstrates that the ensemble mean recovers slightly but consistently more than the no-wave condition. The wake centers are seen to recover only about 43% by 5D. The phase averaged wake centers are seen to oscillate about the ensemble mean as the wake recovers. This indicates that there is a periodicity, or a speeding up and slowing down, to the recovery. This is in agreement with what was seen for  $\bar{u}_\phi/\bar{u}_\infty$  and supports the wake pumping rationale. One full oscillation is slightly longer than one 2.3D wavelength. For example, phase ( $\phi$ ) 2 crosses the mean at 1D and crosses for a full oscillation at approximately 4D. These oscillations are more distinct closer to the turbine.

Figure 6.b shows the longer 1.25 Hz wave wake recovery. As before, these oscillations are not as pronounced but are still present. For example, a half-period for this wave is approximately 3.3D, and both phase ( $\phi$ ) 2 and 4 are both very close to the ensemble mean at 1D and first cross it at approximately 4D downstream. Further, phase 2 and 4 are symmetric with one at a crest and the other at a trough, which again suggests the pumping effect of the long period wave. It is reasonable to assume that the amplitude of these

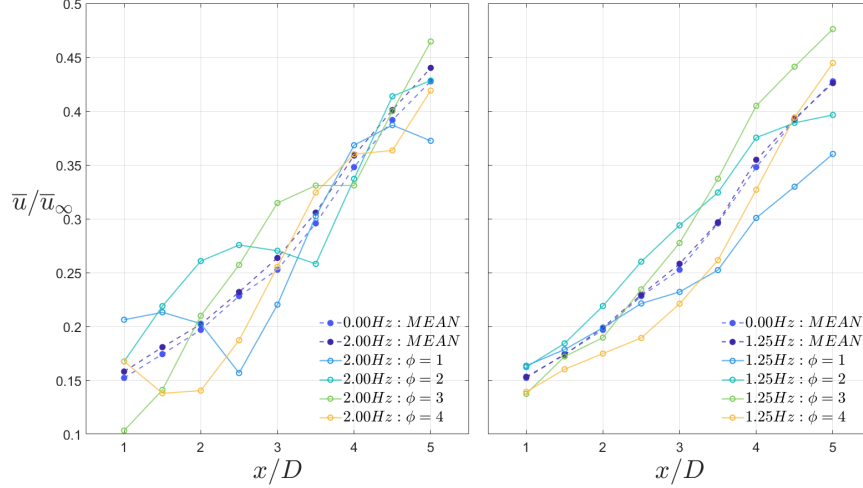


Figure 6: Wake Recovery ( $\bar{u}/\bar{u}_\infty$ ) at selected points for no-wave condition ensemble mean (MEAN), full-wave ensemble mean (MEAN), and phases 1-4 ( $\phi=1 - 2$ ): a) short period wave (2.00 Hz), and b) long period wave (1.25 Hz).

oscillations for Figure 6 is dampened as the wake moves downstream but this is difficult to confirm due to the length of the wave.

### 6.3 Wake Center Deviation

The wake center deviation is presented in Figures 7.a and 7.b. Probe points and window size is the same as the wake recovery, with the turbine hub height at zero. In Figure 7.a the no wave condition diverges down toward water level from the ensemble mean. This suggests that the ensemble mean wake center may be forced higher by vertical shear and momentum flux. The oscillation mentioned for the recovery in Figure 6.a is even more stark for the deviation in Figure 7.a. For example, phase 3 starts at the mean at 2D and

completes one wavelength around  $4.3D$ , which is expected for a wavelength of  $2.3D$ . Note that these oscillations are present for all phases but phase 4 does not cross the mean as expected. This could be due to the turbulent nature of the flow or a low number of images in the data set.

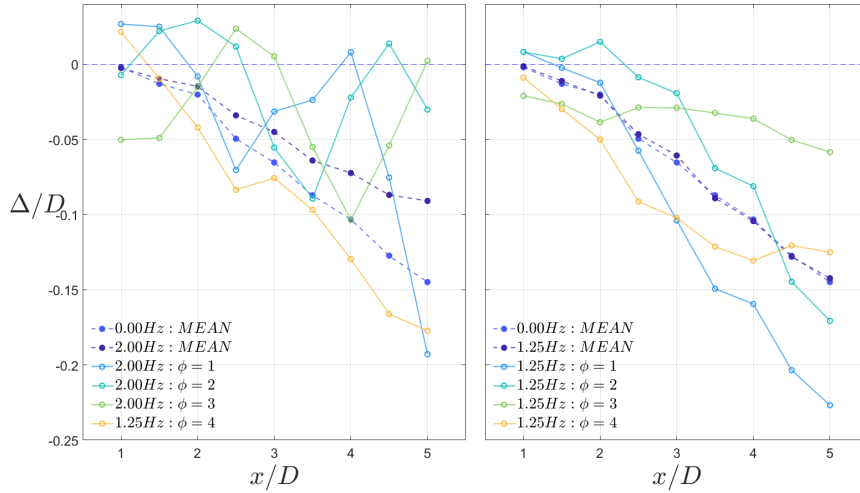


Figure 7: Wake center deflection normalized by rotor diameter ( $\Delta/D$ ) at selected points for no-wave condition ensemble mean (MEAN), with waves ensemble mean (MEAN), and phases 1-4 ( $\phi=1-4$ ): a) short period wave (2.00 Hz), and b) long period wave (1.25 Hz).

Figure 7.b displays the longer 1.25 Hz wave wake-center deviation. Unlike the results from the 2 Hz wave, the mean and the no-wave condition align nicely for the 1.25 Hz wave in Figure 7.b. This aligns with the vertical shear seen downstream in Figures 9.(a, b). The oscillations are in line with the wavelength as can be seen for phase 2 in Figure 7.b. Phase 2 crosses the mean at approximately  $1D$  and  $4.3D$  for giving a half wavelength of  $3.3D$  which is expected for the 1.25 Hz wave.

As the wake center recovery shows, there is periodic effect behind the turbine in the low pressure region directly behind the hub. This can provide additional stresses on the turbine over its life, as well as downstream turbines. In order to provide a more complete picture of downstream turbine effects and modeling, the fluctuating effects seen in the wake recovery will need to be accounted for. Depending on conditions, this would result in an underprediction or overprediction of power output. Not only is the horizontal velocity component seen in the wake recovery oscillating, so is the vertical position of that oscillation. This means that the wake is experiencing a multi-directional undulation, which is wind and wave-phase dependent.

## 6.4 Vertical Velocity

Figures 8.a and 8.b present the ensemble-averaged vertical velocity profiles ( $\bar{v}/\bar{v}_\infty$ ) for wave frequencies of 2 Hz and 1.25 Hz, respectively. Figure 8.b reveals positive vertical velocity components on the lower region of plane 2 and 3, and an opposing negative velocity in the upper portion. The intersection of the positive and negative components is caused by entrainment into the wake as it recovers. A vertical velocity of zero is slightly below where the wake center is for the long wavelength (1.25 Hz) wave but the positive vertical velocity drifts away from the water level as it moves from plane 2 to plane 3 in Figures 8.a, which again, may be due to the wave pumping action. Plane 1, on the other hand, for both Figures 8.a and 8.b are dominated by positive velocity component. This is likely due to continuity since the incoming flow

is forced around the turbine rotor as is indicated by the negative velocity in the lower-left corner of Figure 8 and the classic tip vortices trailing the top of the turbine blade. The top of the turbine is open to the ABL but the water below the turbine imposes an additional boundary layer interaction and forces the flow back up. Figure 8.a has larger magnitudes in plane 1 and does not exhibit the same negative region seen in the lower-left of Figure 8.b. This is due to the averaging of the wave peaks near the turbine which, through continuity, contribute to the vertical velocity more for the 2 Hz wave frequency.

It should be noted that there is also a vertical velocity contribution from wake rotation. This may interact with the vertical velocity induced by the waves. Also, if the PIV measurement plane is not perfectly in the center of the wake, part of the wake rotation may affect the vertical velocity we see in the measurements. We know that even for a perfectly aligned wind turbine, the wake may deflect sideways due to the interaction with the ground and shear in the boundary layer, and this small component of the wake rotation could be showing up in these planes. However, as seen next, the velocity from the short waves is very strong and distinct.

Figures 8.c and 8.d present the conditional (phase-averaged) velocity means  $(\bar{v}_\phi/\bar{v}_\infty)$  for the first of four phases considered, and as before, they show the short wavelength (2 Hz) and longer (1.25 Hz) wavelength, respectively. Figure 8.c exhibits distinct positive high-velocity lobes at the leading edge of each wave crest with alternating negative velocity lobes at the trailing

edge of the waves. Due to continuity, the streamwise velocity seen in Figure 5.c is deflected vertically in Figure 8.c at the front of the wave, then speeds up horizontally at the wave crest indicated by the zero vertical velocity, and finally becomes negative vertical velocity as the flow recovers. The vertical velocities in Figure 8.d are less distinct and more turbulent than in Figure 8.c, but there is still a strong positive component at the leading edge of the wave that can be seen.

The phase-averaged 2 Hz velocity profiles ( $\bar{v}_\phi/\bar{v}_\infty$ ) for phases 1-4 are presented in Figures 8.c, 8.e, 8.g, and 8.i respectively. The extremely distinct positive lobes in Figure 8.c distinctly follow the waves downstream at each wave phase as can be seen in each successive Figure 8.e, 8.g, and 8.i. The lobes at the leading edge of the second wave in the figures are slightly diminished as the wave moves downstream retain their magnitude more than the high velocity regions in the streamwise direction (Fig. 5.c, 5.e, 5.g, and 5.i). This again, may be due to the pumping of the wave. It is worth noting that since the turbine is located at  $x/D = 0$ , there is a portion of the flow around the turbine rotor that is not seen. Therefore, continuity can still play a part in the large positive regions as described previously even though there is a negative lobe visible in the lower left of Figure 8.i.

Figures 8.f, 8.h, and 8.j) display a continuation of the trends described in Figure 5.d. The vertical velocity in Figures 8.d, 8.f, 8.h, 8.j is marked by the passing of the wave. The positive regions follow the 1.25 Hz wave from the leading edge up to the crest as is seen for the 2 Hz waves. And when the

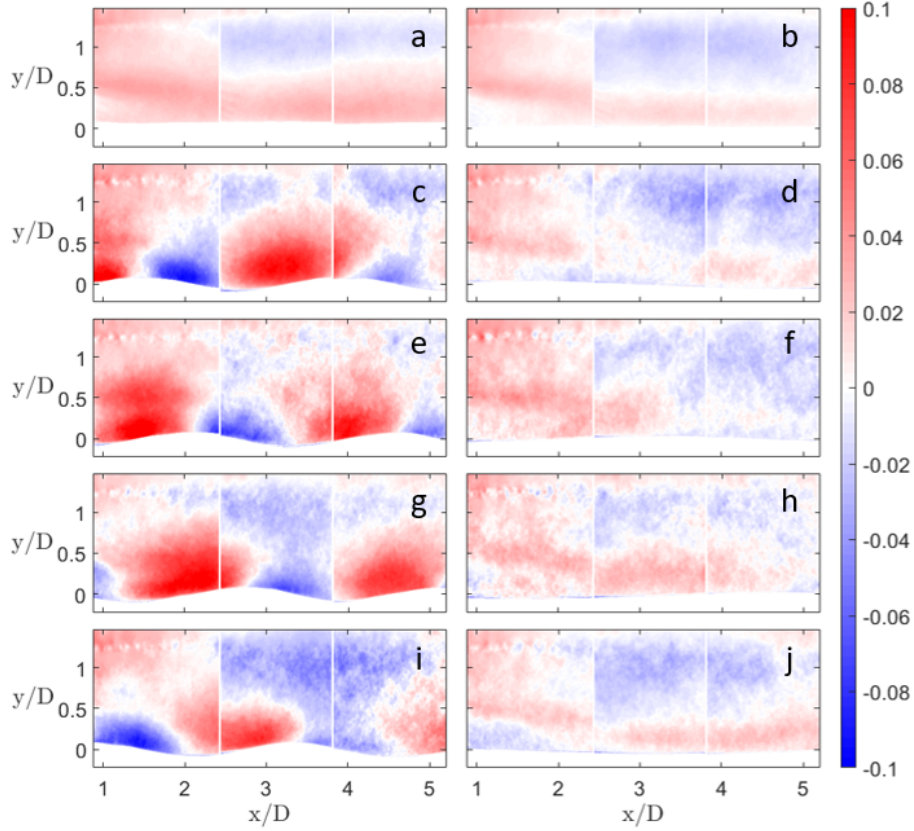


Figure 8: Normalized vertical velocity profiles for 5.9 m/s inflow: (a) ensemble-average for 2 Hz wave and (b) ensemble-average for 1.25 Hz wave and (c) phase-average,  $\phi = 1$ , for 2 Hz wave and (d) phase-average,  $\phi = 1$ , for 1.25 Hz wave and (e) phase-average,  $\phi = 2$ , for 2 Hz wave and (f) phase-average,  $\phi = 2$ , for 1.25 Hz wave and (g) phase-average,  $\phi = 3$ , for 2 Hz wave and (h) phase-average,  $\phi = 3$ , for 1.25 Hz wave and (i) phase-average,  $\phi = 4$ , for 2 Hz wave and (j) phase-average,  $\phi = 4$ , for 1.25 Hz wave.

flow from the top is large in magnitude, it tends to be small at the wave and vice versa.

The considerations outlined in this section, again, have design implications. While vertical momentum surely has an effect on structural and life-

cycle design. The power extraction implications are clear, if the wake pumping is converting horizontal momentum to vertical momentum, the turbine will only be able to utilize some diminished component of momentum orthogonal to the rotor plane. This suggests, for example, that forward tilted or pitch-actuated turbine designs to harness vertical momentum, could help with power generation. The increase in vertical momentum suggests that the wake will remain horizontal longer downstream. This would counteract the natural benefit of wake meandering toward water-level, which would affect spacing requirements. Since there is strong coherence formed along the wake and is phase dependent, these structures will inevitably influence the downstream turbines. These effects may be counteracted by a floating turbine or potentially be exacerbated. In either case, more complex control algorithms would be helpful for the case of a floating wind turbines.

## 6.5 Turbulent Shear

Figures 9.a and 9.b display the normalized ensemble-averaged turbulent shear contours ( $\overline{u'v'}_\phi/u_\infty^2$ ) for wave frequencies of 2 Hz and 1.25 Hz, respectively. There is a region at turbine hub height where the shear stress is zero and switches sign. This aligns nicely with the streamwise wake center produced in Figures 5.a, and 5.b. High values of negative and positive shear stress are seen at the top and bottom tip height of the rotor. Downstream, the regions of negative and positive shear stress spread out as the wake recovers through turbulent mixing. Both figures are very similar with the exception of the

negative turbulent flux in Figure 8.a, which spans the wave average between planes 1 and 2.

The normalized conditional (phase-averaged) turbulent shear  $\overline{u'v'}_\phi/u_\infty^2$  is presented in Figures 9.c and 9.d for plane 1. As with the ensemble means, zero shear stress is coupled with the wave shape similar to the streamwise wake center Figure 5. The shear stress is also less uniform directly behind the turbine rotor in both cases and more so downstream. Near the wave, however, the longer wavelength (Fig. 9.d), reveals that the stress remains the same throughout, while for the shorter period the Reynolds shear stress is positive prior to the crest and negative after (Fig. 9.d). This is in agreement with the mean vertical velocity, which seems to be strongly linked with the Reynolds stress signature.

The normalized phase-averaged Reynolds stresses ( $\overline{u'v'}_\phi/u_\infty^2$ ) for phases 1-4 of the short period wave are presented in Figures 9.c, 9.e, 9.g and 9.i, respectively. As we have seen for the velocity components, the progression of the images confirms that the turbulent shear profile aligns with the phase-locked wave profile. This progression is also seen with the positive shear sections near the leading edge of the 2 Hz waves, followed by the a negative stress at the trailing edges. The more pronounced negative shear region near the turbine of 9.c extends to approximately 2.3D and is seen to progress downstream through Figures 9.(e, g, i) ending at approximately 4.5D (Fig. 9.i). Undulations are visible throughout, especially close to the turbine. Even the negative shear layer at the top is affected by the waves, which can be

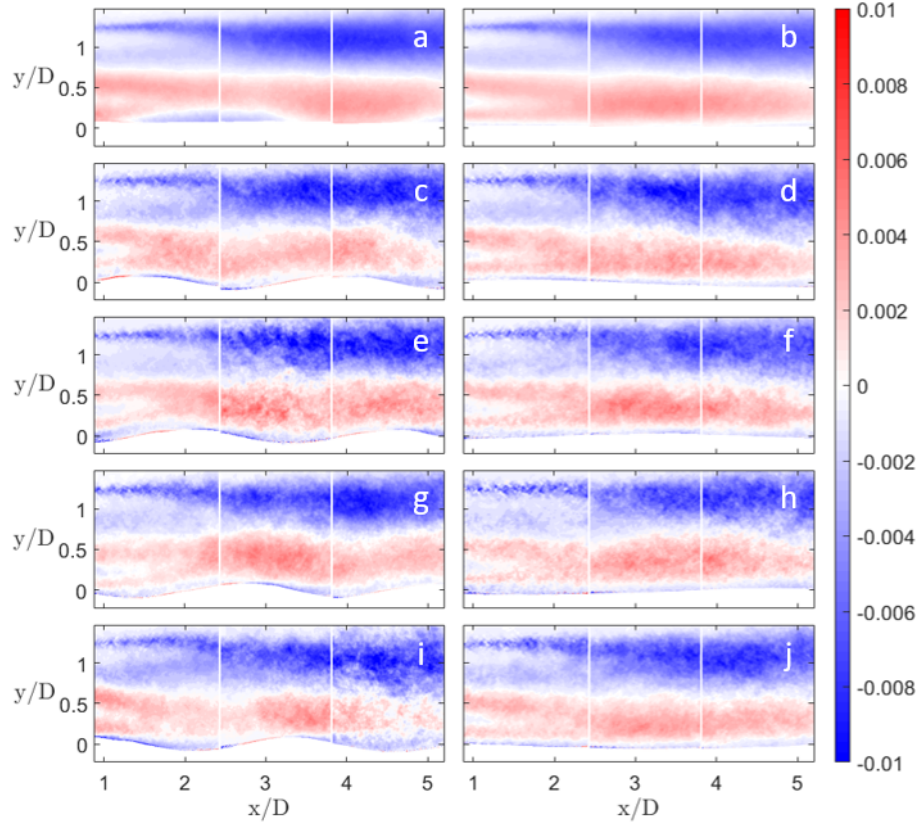


Figure 9: Normalized Reynolds Shear Stress  $\overline{u'v'}_\phi/u_\infty^2$ : (a) ensemble-average for 2 Hz wave and (b) ensemble-average for 1.25 Hz wave and (c) phase-average,  $\phi = 1$ , for 2 Hz wave and (d) phase-average,  $\phi = 1$ , for 1.25 Hz wave and (e) phase-average,  $\phi = 2$ , for 2 Hz wave and (f) phase-average,  $\phi = 2$ , for 1.25 Hz wave and (g) phase-average,  $\phi = 3$ , for 2 Hz wave and (h) phase-average,  $\phi = 3$ , for 1.25 Hz wave and (i) phase-average,  $\phi = 4$ , for 2 Hz wave and (j) phase-average,  $\phi = 4$ , for 1.25 Hz wave.

seen in Figures 9.e and 9.g. This is surprising since the wave is playing a role in the Reynolds stress occurring as far away as the top tip of the turbine rotor.

Figures 9.f, 9.h, and 9.j also demonstrate a continuation of the trends

described in Figure 9.d. The shear profile becomes less turbulent as the wave moves downstream and follows the concavity of the wave shape. The upper region of negative shear near the turbine does not seem to travel with the wave as much as for the short period wave. The positive shear regions at the leading edge of the wave followed by the negative shear at the trailing edge seen in Figures 8.c, 8.e, 8.g, and 8.i are not present for the long period wave, demonstrating a consistent layer of negative shear near the wind-wave interface.

Energy extraction from the turbine is related to the turbulent momentum flux and has a strong phase dependence on  $\overline{u'v'}$ . The positive shear in the lower portion of the turbine suggests using control mechanisms, which include mechanical phase variations as the power is extracted. This wave dependence can prove detrimental to the life cycle of the turbine, especially if the effects are coupled with the blade passage as the waves progresses downstream.

## **6.6 Phase-Averaged Wave-Induced Reynolds Normal Stress**

The preceding analysis has shown a qualitative phase dependence for the phase-averaged velocity (Fig. 5 and 8) and shear stress (Fig. 9), as well as a quantitative phase dependence for the phase-averaged wake recovery (Fig. 6) and deviation (Fig. 7). To further explore and quantify the phase dependence of Reynolds stresses on the ocean waves, the phase-averaged wave-induced

fluctuating term,  $\tilde{u}_\infty(x, y; \phi)$ , from Equation (9) was considered.

Figures 10.a, 10.c, 10.e, and 10.g show the normalized wave-induced normal stress  $\tilde{u}'_\phi \tilde{u}'_\phi / u_\infty^2$  for the high frequency (2 Hz) wave condition. The wave induced stresses in the streamwise direction have large magnitude lobes at both the wave crests, which is consistent with the high velocity regions in the wave-coherent streamwise velocity and troughs, predominantly near the turbine, which is consistent with the reduced velocity regions in the streamwise velocity.

Figures 10.b, 10.d, 10.f, and 10.h display the four phases of  $\tilde{u}'_\phi \tilde{u}'_\phi / u_\infty^2$  for the low frequency (1.25 Hz) wave condition, which have a lower magnitude stress but follow a similar trend to the 2 Hz wave phases. High-stress regions are located at both the crest and troughs of the long-period wave. Unlike the wave-induced stresses in the streamwise direction, the normalized wave-induced vertical normal stresses,  $\tilde{v}'_\phi \tilde{v}'_\phi / u_\infty^2$ , are dramatically different between the high-frequency and low-frequency wave conditions seen in Figures 11.a, 11.c, 11.e, and 11.g and 11.b, 11.d, 11.f, and 11.h, respectively. Similar to the phase-averaged vertical velocity profiles from Figure (8), the 2 Hz wave shows high-stress regions at the leading, upwind, edge of the waves as well as downwind of the wave. These high-stress lobes are synchronized with the high-frequency wave as it moves downstream.

However, the wave-induced vertical stresses are virtually non-existent for the long period (1.25 Hz) waves. This is in stark contrast to the phase-averaged shear stresses which are comparable between the wave frequen-

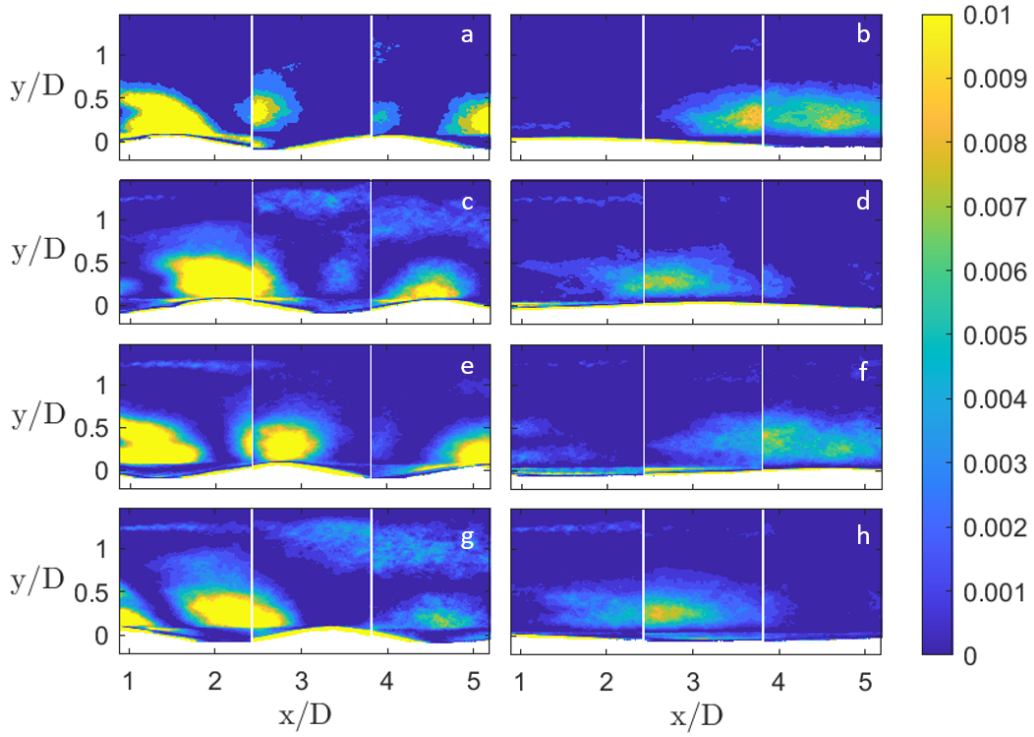


Figure 10: Normalized phase-averaged wave-induced streamwise normal stress ( $\tilde{u}'_{\phi}\tilde{u}'_{\phi}/u_{\infty}^2$ ) for 5.9 m/s inflow: (a) wave-induced stress,  $\phi = 1$ , for 2 Hz wave and (b) wave-induced stress,  $\phi = 1$ , for 1.25 Hz wave and (c) wave-induced stress,  $\phi = 2$ , for 2 Hz wave and (d) wave-induced stress,  $\phi = 2$ , for 1.25 Hz wave and (e) wave-induced stress,  $\phi = 3$ , for 2 Hz wave and (f) wave-induced stress,  $\phi = 3$ , for 1.25 Hz wave and (g) wave-induced stress,  $\phi = 4$ , for 2 Hz wave and (h) wave-induced stress,  $\phi = 4$ , for 1.25 Hz wave.

cies. As noted previously, this suggests that the high-frequency waves have a strong vertical influence on the turbine wake.

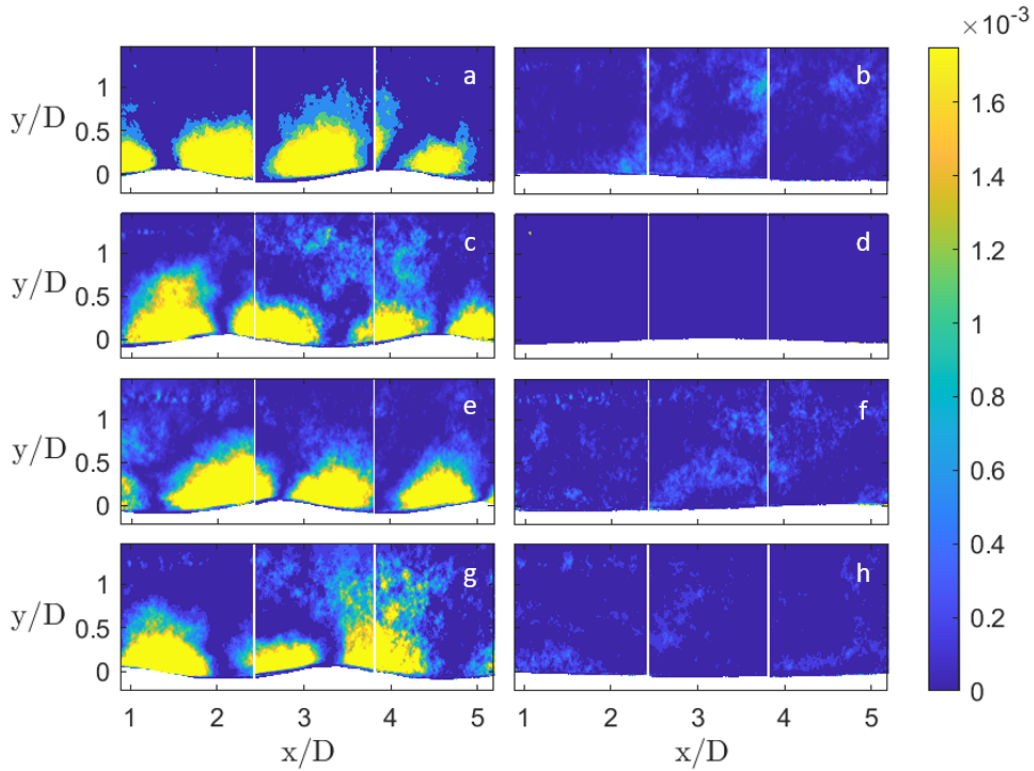


Figure 11: Normalized phase-averaged wave-induced vertical normal stress ( $\tilde{v}'_{\phi} \tilde{v}'_{\phi} / u_{\infty}^2$ ) for 5.9 m/s inflow: (a) wave-induced stress,  $\phi = 1$ , for 2 Hz wave and (b) wave-induced stress,  $\phi = 1$ , for 1.25 Hz wave and (c) wave-induced stress,  $\phi = 2$ , for 2 Hz wave and (d) wave-induced stress,  $\phi = 2$ , for 1.25 Hz wave and (e) wave-induced stress,  $\phi = 3$ , for 2 Hz wave and (f) wave-induced stress,  $\phi = 3$ , for 1.25 Hz wave and (g) wave-induced stress,  $\phi = 4$ , for 2 Hz wave and (h) wave-induced stress,  $\phi = 4$ , for 1.25 Hz wave.

## 6.7 Phase-Averaged Wave-Induced Reynolds Shear Stress

Some differences between the ensemble stress and the phase-averaged shear stresses have been explored in the previous sections but the magnitude of that difference, or fluctuation, can be visualized by the wave-induced tur-

bulent stress  $\tilde{u}'_\phi \tilde{v}'_\phi / u_\infty^2$ . The 2 Hz wave seen in Figures 12.a, 12.c, 12.e, and 12.g reveals regions of positive and negative wave-induced shear located at the upwind and downwind faces of the wave, respectively. These regions are of comparable magnitude with the phase-averaged shear in Figure (9), suggesting that the wave has a large effect on the phase-averaged shear stress ( $u'_\phi v'_\phi / u_\infty^2$ ). The stress, and therefore the effect, is diminished downstream but is still relatively strong at the leading (upwind) edge of the 2 Hz wave.

The long period wave (1.25 Hz) in Figures 12.b, 12.d, 12.f, and 12.h produces much smaller regions of shear stress but what is present follows the same trend of being located at the leading and trailing edges of the wave. Notably, the order of magnitude for the 1.25 Hz wave  $\tilde{u}'_\phi \tilde{v}'_\phi / u_\infty^2$  is also comparable to the phase-averaged stresses  $u'_\phi v'_\phi / u_\infty^2$ . This means that, even though the effect covers a smaller region, the strength of the wave-induced shear is nevertheless significant. It is interesting to note that the lobe values in Figure 12.g are flipped in sign about the wave crest at  $x/D \approx 3.2$  from what is expected. This is likely due to the wake recovery undulation (Fig. 6) and suggests a slightly negative streamwise velocity fluctuation ( $u'_4$ ) or recirculation near the turbine, since the wave-induced fluctuation  $\tilde{u}'_4$  is likely positive in that region.

The wave-induced stresses suggest that the wave frequency plays a pivotal role for design considerations. While phase-dependent coupling is clearly present between the turbine wake and high frequency (2 Hz) waves, this relationship is not as clear for the low frequency (1.25 Hz) waves. Specifically,

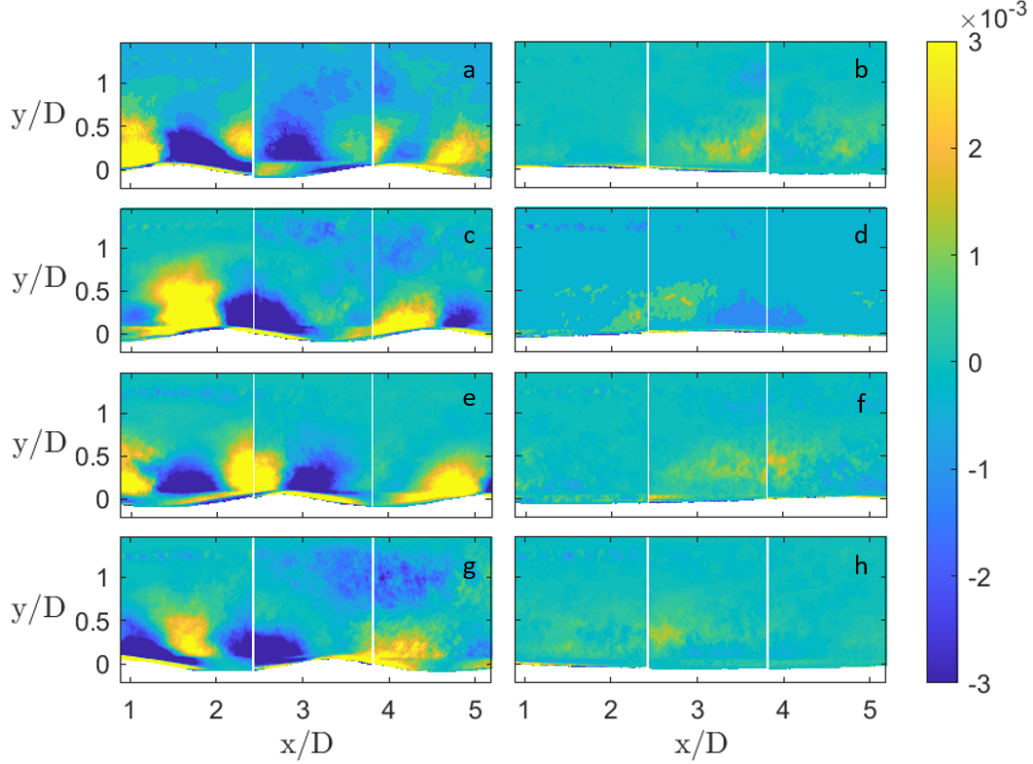


Figure 12: Normalized phase-averaged wave-induced shear stress ( $\tilde{u}'_\phi \tilde{v}'_\phi / u_\infty^2$ ) for 5.9 m/s inflow: (a) wave-induced shear,  $\phi = 1$ , for 2 Hz wave and (b) wave-induced shear,  $\phi = 1$ , for 1.25 Hz wave and (c) wave-induced shear,  $\phi = 2$ , for 2 Hz wave and (d) wave-induced shear,  $\phi = 2$ , for 1.25 Hz wave and (e) wave-induced shear,  $\phi = 3$ , for 2 Hz wave and (f) wave-induced shear,  $\phi = 3$ , for 1.25 Hz wave and (g) wave-induced shear,  $\phi = 4$ , for 2 Hz wave and (h) wave-induced shear,  $\phi = 4$ , for 1.25 Hz wave.

the low frequency waves show an influence on both the wave-induced stream-wise normal stress ( $\tilde{u}'_\phi \tilde{u}'_\phi$ ) and the wave-induced shear stress ( $\tilde{u}'_\phi \tilde{v}'_\phi$ ), but are virtually non-existent for the wave-induced vertical normal stress ( $\tilde{v}'_\phi \tilde{v}'_\phi$ ). On the other hand, the high-frequency 2 Hz waves show an overwhelming coupling between the wave profile and the wave-induced stresses for all terms. In

fact, the most dramatic disparity between the wave-induced stresses is that of the  $\tilde{v}'_\phi \tilde{v}'_\phi$  terms seen in the left and right side of Figure (11). This suggests that the relative wind speed versus wave speed, or frequency, is a factor in the magnitude of the vertical component of the normal and shear stresses, which ultimately influences the turbine wake.

## 6.8 Advection-Turbulence Profiles

Figures 13.a and 13.b show the advection and turbulence profiles from Equation (7) at  $\phi = 1$  ( $x/d = 1$ ). For both wave conditions, the advective terms are negative below hub height ( $y/D \approx 0.7$ ), and the turbulence terms are positive. Above hub height, the sign of the terms is reversed with positive advection and negative turbulence for the means. Close to the wave ( $y/D \approx 0.1$ ), the signal is noisy and does not have meaningful interpretation. Both terms quickly become very positive at  $y/D \approx 1.2$ , back to very negative at  $y/D \approx 1.3$ , and tend to zero as the flow approaches free-stream velocity. This sudden change is due to entrainment at the edge of the wake and is greater in magnitude for the 1.25 Hz wave in Figure 13.b. This may be due to less disruption of the wake by wake pumping as we have seen in the velocity and shear contours.

While Figure 13.b has a slight oscillation about the mean for the advection peak and trough, the remaining terms are very close to both the advective and turbulent mean. However, the high frequency wave in Figure 13.a reveals a dramatic divergence between the peak and trough ( $\phi = 12$ ) at  $y/D \approx 0.5$ .

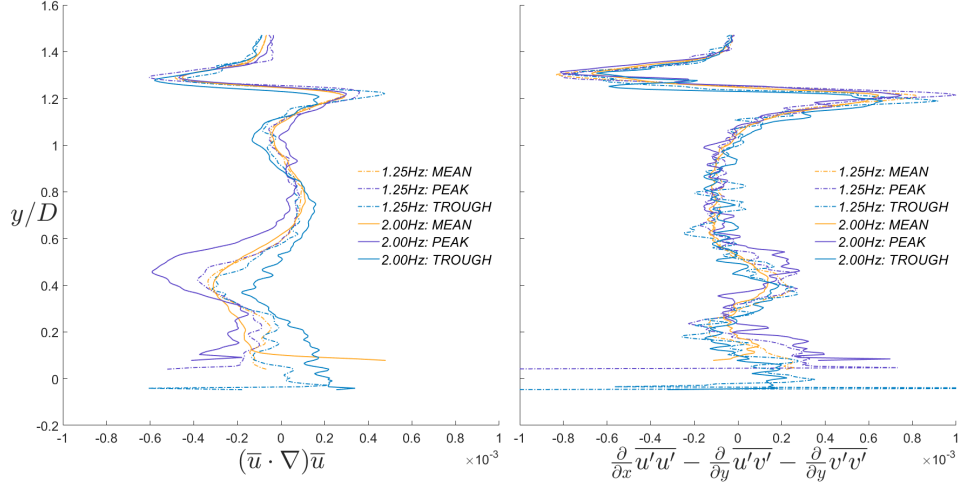


Figure 13: Advection (A) Turbulence (T) Profiles at  $x/D=1.5$  for different  $y/D$  locations. Includes ensemble mean (MEAN),  $\phi = 1$  (PEAK), and  $\phi = 3$  (TROUGH): a) short period wave (2.00 Hz), and b) long period wave (1.25 Hz).

The turbulence terms for the 2 Hz wave diverge about the mean as well but are generally noisier and fluctuate throughout the vertical profile, which is expected.

Since the streamwise advection disparity between peak and trough is most prominent below turbine hub height at approximately  $y/D = 0.7$ . This reinforces the notion that a discrepancy between the upper half of the turbine rotor and the lower half needs to be accounted for during design. From an engineering perspective, it also suggests an opportunity. As stated before, some controls, siting, modeling, and optimization implications could be used to utilize energy extraction from the localized bulk fluid motion. The Reynolds stresses further support these implications since similar phase de-

pendence is seen at a similar turbine height. The phase dependent stresses also confirm that looking at only the ensemble stresses provides a limited view, from a design perspective, of all the dynamics contained in the system.

## 7 Conclusion

This experiment considered a scaled fixed-bottom wind turbine under two wind conditions and three wave conditions inside an augmented wind tunnel, retrofitted with a wave-generating wave tank. PIV measurements were collected at three separate downstream locations to generate the velocity fields directly behind, and far downstream, of the turbine. The PIV snapshots were also used to detect the instantaneous wave profiles and used to sort the velocity fields into like wave-phase averages. The wave-phase averages, as well as the full ensemble averages, were then used to calculate the wake center profiles, mean streamwise velocities ( $\bar{u}_\phi/\bar{u}_\infty$ ), mean vertical velocities ( $\bar{v}_\phi/\bar{v}_\infty$ ), and Reynolds shear stress  $\overline{u'v'_\phi}/\bar{u}^2$ . The wake center positions were also used to quantify wake recovery as well as wake-center deviation. Finally, the advection and turbulence term profiles were calculated at  $x/D = 1.5$ .

The streamwise velocity results revealed a clear dependence on the wake profile to the location, or phase, of the wave. Localized velocity maxima at the wave crests were established due to the pumping behavior of the waves, with larger velocity magnitudes near the turbine. This revealed that ensemble averages show an incomplete and more placid view of the underlying

dynamics of the wake development and recovery. These effects were amplified for the higher frequency ( $2Hz$ ) wave condition. The phase dependence on the vertical velocity was also confirmed. Both wave frequencies showed this dependence but the higher frequency wave exhibited a more dramatic result, with distinctly larger magnitudes for the full length of the experiment. Further, for this frequency ( $2Hz$ ) the ensemble average showed that the vertical (positive) velocity component completely dominates the region directly behind the turbine and is seen increasing vertically downstream. Reynolds shear stress was shown to be correlated with the phase as well, and extended to the top of the wind turbine. The higher positive shear near the bottom indicate an imbalance of stresses on the turbine which has many design implications.

The phase dependent recovery values at wake center, illustrate that wake pumping is responsible for the horizontal speeding up and slowing down of the wake recovery. Furthermore, the vertical wake-center deviation is also phase dependent and therefore establishes a multi-directional oscillation, which is coupled with the wind and wave characteristics. As seen from the momentum budget profiles, bulk fluid motion through advection has a prominent distinction between the peak and trough of a wave at  $x/D = 1$ . This reinforces the disparity between the lower and upper portion of the turbine and should be considered in turbine design.

The phase-averaged wave-induced stresses not only confirm the wave-wake coupling but further distinguish the differences between the vertical

component of the Reynolds stresses and the wave frequency. At the same inflow conditions ( $5.9m/s$ ), the wave speed ( $1.2m/s$  or  $1.25$  Hz) closer to the inflow speed showed a significantly smaller effect on vertical stress compared to the slower  $0.7m/s$  wave speed, which had a very strong effect on all Reynolds stresses.

In order to gain a complete picture of wind-wave-wake dynamics, the spacial and temporal coupling of these effects must be considered. Localized momentum and stress undulations present a host of considerations for optimization, siting, modeling, and maximizing power production. The wave motion does not necessarily add momentum to the wake but changes the horizontal inflow momentum (streamwise) to vertical. A single fixed turbine was selected as a starting point for this discussion.

Further experimental studies have a broad selection of topics to investigate. Such as, how much power production is lost due to the vertical displacement of the incoming momentum, how does that displacement effect wake recovery, what bandwidth of resonant frequencies can the wind-wave coupling produce, what control schemes may be useful to maximize power extraction, what spacing is optimal, what structural consideration need to be taken, what are the critical wind versus wave speed ratios, and so on. For instance, a study should look at the characteristics and power production of a fixed turbine model directly downstream of another. This would help illuminate the magnitude of the phenomena discussed in this study. This can, of course, be extended to entire wind farms, floating wind farms,

tilted turbines, etc. Further study will be needed to fully characterize this complex interaction between wind, turbines, and waves for a full wind-farm application.

## 8 References

- [1] Espen Åkervik and Magnus Vartdal. “The role of wave kinematics in turbulent flow over waves”. In: *arXiv preprint arXiv:1901.11319* (2019).
- [2] S Baidya Roy, Stephen Wilson Pacala, and RL Walko. “Can large wind farms affect local meteorology?” In: *Journal of Geophysical Research: Atmospheres* 109.D19 (2004).
- [3] Jacob Berg et al. “Large-eddy simulation of turbine wake in complex terrain”. In: *Journal of Physics: Conference Series*. Vol. 854. 1. IOP Publishing, 2017, p. 012003.
- [4] Juliaan Bossuyt, Charles Meneveau, and Johan Meyers. “Effect of layout on asymptotic boundary layer regime in deep wind farms”. In: *Physical Review Fluids* 3.12 (2018), p. 124603.
- [5] Juliaan Bossuyt, Charles Meneveau, and Johan Meyers. “Wind farm power fluctuations and spatial sampling of turbulent boundary layers”. In: *Journal of Fluid Mechanics* 823 (2017), pp. 329–344.

- [6] S-P Breton et al. “A survey of modelling methods for high-fidelity wind farm simulations using large eddy simulation”. In: *Philosophical Transactions of the Royal Society A: Mathematical, Physical and Engineering Sciences* 375.2091 (2017), p. 20160097.
- [7] Marc P Buckley and Fabrice Veron. “The turbulent airflow over wind generated surface waves”. In: *European Journal of Mechanics-B/Fluids* 73 (2019), pp. 132–143.
- [8] Tony Burton et al. *Wind energy handbook*. Vol. 2. Wiley Online Library, 2001.
- [9] Raúl Bayoán Cal et al. “Experimental study of the horizontally averaged flow structure in a model wind-turbine array boundary layer”. In: *Journal of Renewable and Sustainable Energy* 2.1 (2010), p. 013106.
- [10] Marc Calaf, Charles Meneveau, and Johan Meyers. “Large eddy simulation study of fully developed wind-turbine array boundary layers”. In: *Physics of fluids* 22.1 (2010), p. 015110.
- [11] Shu-Hsien Chou et al. “Air-sea fluxes retrieved from Special Sensor Microwave Imager data”. In: *Journal of Geophysical Research: Oceans* 102.C6 (1997), pp. 12706–12726.
- [12] Antonio Crespo, J Hernandez, and Sten Frandsen. “Survey of modelling methods for wind turbine wakes and wind farms”. In: *Wind Energy: An International Journal for Progress and Applications in Wind Power Conversion Technology* 2.1 (1999), pp. 1–24.

- [13] Paris IEA. “World wind electricity production by region”. In: <https://www.iea.org/data-and-statistics/charts/world-wind-electricity-production-by-region-2005-2018> (2020).
- [14] A Jimenez et al. “Advances in large-eddy simulation of a wind turbine wake”. In: *Journal of Physics: Conference Series*. Vol. 75. 1. IOP Publishing. 2007, p. 012041.
- [15] A Jimenez et al. “Large-eddy simulation of spectral coherence in a wind turbine wake”. In: *Environmental Research Letters* 3.1 (2008), p. 015004.
- [16] Yi Liu et al. “Numerical study of pressure forcing of wind on dynamically evolving water waves”. In: *Physics of Fluids* 22.4 (2010), p. 041704.
- [17] Davide Medici and PH Alfredsson. “Measurements on a wind turbine wake: 3D effects and bluff body vortex shedding”. In: *Wind Energy: An International Journal for Progress and Applications in Wind Power Conversion Technology* 9.3 (2006), pp. 219–236.
- [18] “Monthly Energy Review and Electric Power Monthly”. In: *Boundary-Layer Meteorology* (February 2021).
- [19] Ylva Odemark and Jens HM Fransson. “The stability and development of tip and root vortices behind a model wind turbine”. In: *Experiments in fluids* 54.9 (2013), p. 1591.

- [20] Yuji Ohya. “Wind-tunnel study of atmospheric stable boundary layers over a rough surface”. In: *Boundary-Layer Meteorology* 98.1 (2001), pp. 57–82.
- [21] Yuji Ohya, David E Neff, and Robert N Meroney. “Turbulence structure in a stratified boundary layer under stable conditions”. In: *Boundary-Layer Meteorology* 83.1 (1997), pp. 139–162.
- [22] Madison J Post et al. “The Combined Sensor Program: an air–sea science mission in the central and western Pacific Ocean”. In: *Bulletin of the American Meteorological Society* 78.12 (1997), pp. 2797–2816.
- [23] Abraham Savitzky and Marcel JE Golay. “Smoothing and differentiation of data by simplified least squares procedures.” In: *Analytical chemistry* 36.8 (1964), pp. 1627–1639.
- [24] Sina Shamsoddin and Fernando Porté-Agel. “Large-eddy simulation of atmospheric boundary-layer flow through a wind farm sited on topography”. In: *Boundary-layer meteorology* 163.1 (2017), pp. 1–17.
- [25] Brian Snyder and Mark J Kaiser. “A comparison of offshore wind power development in Europe and the US: Patterns and drivers of development”. In: *Applied Energy* 86.10 (2009), pp. 1845–1856.
- [26] Michael A Sprague et al. “ExaWind: A multifidelity modeling and simulation environment for wind energy”. In: *Journal of Physics: Conference Series*. Vol. 1452. 1. IOP Publishing. 2020, p. 012071.

- [27] Luong Van Binh et al. “A peak factor for non-Gaussian response analysis of wind turbine tower”. In: *Journal of Wind Engineering and Industrial Aerodynamics* 96.10-11 (2008), pp. 2217–2227.
- [28] LJ Vermeer, Jens Nørkær Sørensen, and Antonio Crespo. “Wind turbine wake aerodynamics”. In: *Progress in aerospace sciences* 39.6-7 (2003), pp. 467–510.
- [29] Yu-Ting Wu and Fernando Porté-Agel. “Large-eddy simulation of wind-turbine wakes: evaluation of turbine parametrisations”. In: *Boundary-layer meteorology* 138.3 (2011), pp. 345–366.
- [30] Shuolin Xiao and Di Yang. “Large-Eddy Simulation-Based Study of Effect of Swell-Induced Pitch Motion on Wake-Flow Statistics and Power Extraction of Offshore Wind Turbines”. In: *Energies* 12.7 (2019), p. 1246.
- [31] Di Yang, Charles Meneveau, and Lian Shen. “Dynamic modelling of sea-surface roughness for large-eddy simulation of wind over ocean wavefield”. In: *Journal of Fluid Mechanics* 726 (2013), p. 62.
- [32] Di Yang, Charles Meneveau, and Lian Shen. “Large-eddy simulation of offshore wind farm”. In: *Physics of Fluids* 26.2 (2014), p. 025101.
- [33] Di Yang and Lian Shen. “Simulation of viscous flows with undulatory boundaries: Part II. Coupling with other solvers for two-fluid computations”. In: *Journal of Computational Physics* 230.14 (2011), pp. 5510–5531.

- [34] Xiaolei Yang, Maggie Pakula, and Fotis Sotiropoulos. “Large-eddy simulation of a utility-scale wind farm in complex terrain”. In: *Applied energy* 229 (2018), pp. 767–777.
- [35] Wei Zhang, Corey D Markfort, and Fernando Porté-Agel. “Wind-turbine wakes in a convective boundary layer: A wind-tunnel study”. In: *Boundary-layer meteorology* 146.2 (2013), pp. 161–179.